Sintering behavior of ultra-thin 3D printed alumina lattice structures

Charles Manière, Christelle Harnois, Sylvain Marinel

Sintering behavior of ultra-thin 3D printed alumina lattice structures

Charles Manière[a]*, Christelle Harnois[a], Sylvain Marinel[a]
(a) Normandie Univ, ENSICAEN, UNICAEN, CNRS, CRISMAT, 14000, Caen, France

Keywords
Stereolithography; Ceramics; Sintering; Anisotropy; Simulation; Lattice

Abstract
Ceramic stereolithography or vat photopolymerization is a process allowing the fabrication of ceramic objects with highly complex shapes. Lattices structures are particularly used together with advanced optimization topology tools for the design of printable lightweight shapes with optimized mechanical resistance. If the mechanical resistance of these lattices structures is well controlled at the polymeric state, they can be severely deformed at high temperatures during the sintering stage. The deformation sensitivity of the lattices structures during the sintering should then be determined to include this aspect at the conception stage. The finite element (FEM) simulation of lattices sintering is an interesting solution to anticipate numerically the deformation sensitivity of the lattices and determine their minimum wall thickness. This requires to determine the sintering behavior of the printed green specimens and to take into account the sintering anisotropy, which involves weaker resistance between the layers. In this study the sintering behavior is first determined by multiple-axis dilatometry, modeled analytically and then simulated by the FEM method. Afterward, the sintering simulation of lattices with different wall thicknesses is conducted. This allows testing the simulation tool predictability for each lattices wall thickness and to compare their deformation sensitivity at high temperatures.

Graphical abstract

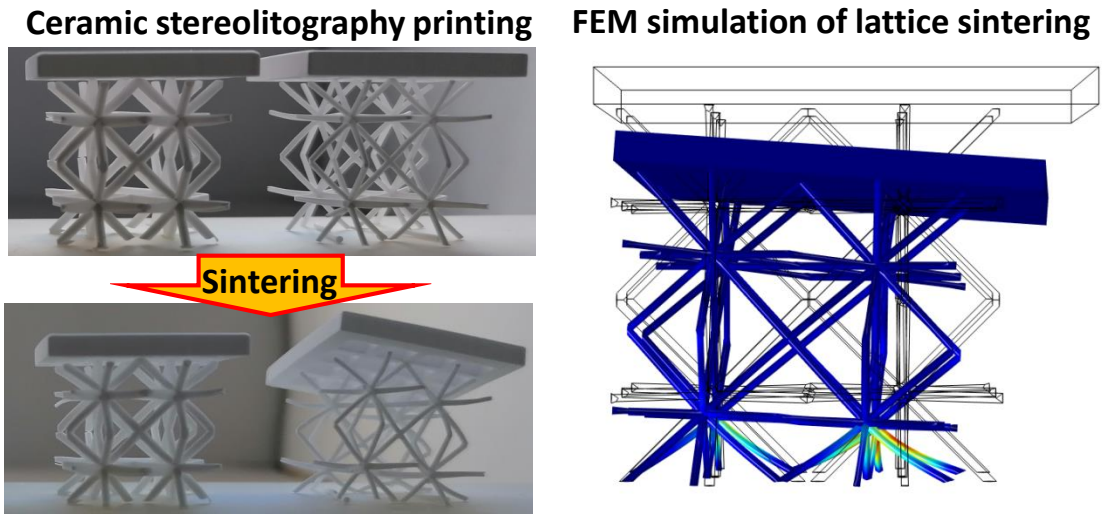

Caption: Exploration of thin, lightweight ceramic lattice resistance to high temperature sintering distortions

Highlights

- Printing resistance of thin lightweight lattice structures
- 3D printed ceramic specimen sintering modeling
- FEM prediction of thin lattice structure high temperature distortion resistance

* Corresponding author: **CM**: Laboratoire de Cristallographie et Sciences des Matériaux (CRISMAT), 6 Blvd du Maréchal Juin 14050 CAEN CEDEX 4, France
Ph.: +33.2.31.45.13.69; *E-mail address*: charles.maniere@ensicaen.fr

Nomenclature

θ Porosity

$\dot{\theta}$ Porosity elimination rate (s^{-1})

$\underline{\sigma}$ Stress tensor ($N.m^{-2}$)

$\underline{\dot{\varepsilon}}$ Strain rate tensor (s^{-1})

$\dot{\varepsilon}_r$ Radial strain rate component (s^{-1})

$\dot{\varepsilon}_z$ Z strain rate component (s^{-1})

φ Shear modulus

ψ Bulk modulus

Pl Sintering stress (Pa)

$\mathbb{i}$ Identity tensor

α Surface energy ($J.m^{-2}$)

r Grain radius (m)

$\dot{e}$ Trace of the strain rate tensor (s^{-1})

η Material viscosity (Pa.s)

K Bulk viscosity (Pa.s)

G Shear viscosity (Pa.s)

η_r Radial component of the viscosity (Pa.s)

η_z Z component of the viscosity (Pa.s)

η_0 Viscosity pre-exponential factor (Pa.s)

η_{0r} Radial component of the viscosity pre-exponential factor (Pa.s)

η_{0z} Z component of the viscosity pre-exponential factor (Pa.s)

Q Viscosity activation energy ($J.mol^{-1}$)

R Gas constant 8.314 ($J.mol^{-1}.K^{-1}$)

T Temperature (K)

1. Introduction

Among the existing additive manufacturing approaches [1–5], ceramic stereolithography is based on the selective UV photopolymerization of a ceramic resin [6–8]. The 3D printed specimens are then debinded (organic removal by burning or dissolution) and sintered in a furnace to densify them[9]. In ceramic stereolithography, the debinding is delicate as the organic content exceeds 50 %. It requires about a week of slow debinding and induces crack formation if the wall thickness exceeds 3-5 mm[10–12]. Consequently, ceramic stereolithography involves a relatively long process. However, the latter is to date one of the oldest and most reliable processes due to the high printing quality/repeatability [13] and the excellent shape resolution (approximately 10–50 µm [14]). Stereolithography is then perfectly suited to the fabrication of thin but highly complex shapes[3]. Together with topology optimization tools[15], stereolitography allows the fabrication of advanced lightweight shapes having complex internal structures, made of lattices[16]. Lattices structures allow optimizing the shape weight while maintaining interesting mechanical resistance[17,18]. Among all existing structures, we can cite the gyroid, octet, diamond or bioinspired structures like bee's honeycomb, trabecular bone[19–21] and even more complex 4D printing structures[22,23]. Lattice structures are used to remove unsolicited areas in thick shapes or as support material in various 3D printing, including stereolitography[16,24].

Compared to pure polymeric shapes, the production of thin ceramic lattices structures or hybrid shapes having internal lattices structures requires addressing an additional challenge which is the debinding/sintering thermal treatment[2,3]. Lattices structures are generally less sensitive to crack formation during debinding because they have thin wall structures[9,10,12]. However, the high temperature of sintering is a stage where the porous specimens have a lower viscosity and are more sensitive to the distortions of their thin structures[25,26]. The modeling[27,28] of the lattice resistance to the sintering stage is then of key importance for the conception of thin structures. In addition, the ceramic stereolithography specimens have layered structures implying anisotropic sintering shrinkage and weaker material resistance

between the layers where higher porosity is present[29–31]. The sintering model of the printed lattices should then account both the densification behavior (in temperature) and the anisotropic behavior of the porous specimen having more compaction in the building direction[29]. In general, the printed specimens have an orthotropic type of anisotropy due to similar sintering behaviors in the two axes of the layer and only a different behavior in the building direction. This orthotropic behavior has been evidenced experimentally by triaxial dilatometry showing sintering shrinkage differences only in the building direction and by microscopy analysis showing architected microstructure containing a higher porosity in the interlayer zone[29–31]. This sintering shrinkage orthotropic behavior has been observed also in other additive manufacturing methods such as robocasting[32], fuse deposition modeling[33,34] or binder jetting[35,36].

In this article, the complex sintering behavior of 3D printed alumina lattices is explored from thick and strong wall structures to very thin (0.25mm) and fragile wall structures. A professional ceramic stereolithography printer with a layer resolution down to (10-50 µm) and a low viscosity ceramic cream has been used to print these very thin and fragile lattices shapes with filling density as low as ~1.6 vol%. In this study, the sintering behavior of the printed alumina is determined on simple shape specimens to extract the temperature/porosity evolution of the printed green specimen with a special attention to the sintering anisotropy. The aim of this study is to verify by loaded lattice buckling sintering tests if the model (*via* FEM simulation) is capable of predicting the complex thin lattice severe distortions at high temperature during the sintering. The onset of severe lattice distortions will be tested for different decreasing wall thicknesses toward the extreme limit of the printing device. This study aims at providing a solution to model weak structures sintering distortions sensitivity.

2. Method

The 3D printing experiments were made on the "CERAMAKER100", a ceramic stereolithography device from 3DCERAM SINTO®. An alumina ceramic cream called "3DMix AL-E02" produced by the manufacturer was used to print the lattices structures. In order to explore the lattice structure resistance to sintering (from strong structures to very thin and fragile structures), we chose a lattice design with rod diameters decreasing from 3mm to 0.5 mm. The latter represents the weakest structure, highly sensitive to the sintering deformation. A simple octet cell reported in figure 1a was used for this study. However, this cell has cutted rods that may behave differently from real lattice made of this cell. Consequently, a geometrically equivalent cell (made of full-rod diameters) was used (see figure 1b). To be less sensitive to the friction with the support, a larger lattice structure made of 8 unit cells was considered. The production plateau of the printed lattices is reported in figure 1c. The printed lattices are made of different rod diameters and their shape contains 45° building rods and cantilever parts on the edges. This tests both the printing limits of the device where less supported and fragile zones may resist the scraping stress during the printing[37] and the limit of the lattices sintering deformation resistance.

The printed lattices were debinded in a tube furnace with an industrial thermal cycle using inert gas for slow (0.1 K/min) debinding without exothermic burning (local overheating) that can generate cracks. The thermal treatment uses different temperatures dwell in the main decomposition stages below 600°C. When reaching 600°C, air was introduced to burn the remaining carbon. After the removal of the organic contents, a subsequent pre-consolidation heating to 1050°C was conducted in air to obtain lattice specimens that can be handled. The debinded specimen was then loaded by a 25×25×2 mm^3 printed green alumina plate placed on the top to increase the lattice deformation sensitivity at high temperatures. The lattices assembly with different rod diameters (from 0.5 to 3 mm) was simultaneously sintered using a fully dense flat alumina support. The sintering cycle in air was 2 K/min heating to 1600°C followed by a 3 h dwell and a cooling at 2 K/min. The aim of the plate loading is to detect the

critical lattice rod diameter where the thin lattice structure severely deforms during sintering stage. The finite element tool (Comsol Multiphysics ®) was used to predict this sintering resistance limit. In the 3D simulation, the lattices and their top plates were assumed merged as one solid. The contact of the lattices and the flat alumina support was simulated as a frictionless slip contact, a reasonable approximation knowing nearly contact points are present at this location in real shapes. In the experiment, the plate manually placed on the top of the lattice were not ideally centered and during the distortions a preferential orientation happens. To force a preferential orientation in the FEM simulations the top plate was voluntarily 2 mm shifted toward a corner.

The sintering densification curves were determined by dilatometry (Seteram TMA96) with a $5\times5\times5$ mm^3 printed cube debinded and sintered with the same cycle. In typical conventional sintering, the cube shrinkage is homothetic and should be the same in all axes. However, the layer structure of 3D printed cubes imply an anisotropy with dissimilar shrinkage between the layer plane and the normal axis to the layers plane. The dilatometry tests recorded the displacement in the printing layers building direction called “Z” and in the radial direction called “R” (in the layers plane) to characterize the sintering anisotropy (orthotropic type). The powder and the sintered microstructures have been analyzed by electronic microscopy SEM (JEOL 7200F).

The main steps of the article simulation strategy is reported in figure 1d. The first step consists of the identification of the anisotropic sintering behavior from multiaxial dilatometry tests on simple cube shape. The second step is the analytic modeling of the dilatometry data and the verification of the FEM simulation tool by the reproduction of the analytic results (*via* the simulation of the cube test). The last step is the parametric simulation of the weighted lattices with rod diameters from 0.5 to 3 mm and the comparison with the equivalent experimental lattice sintering tests.

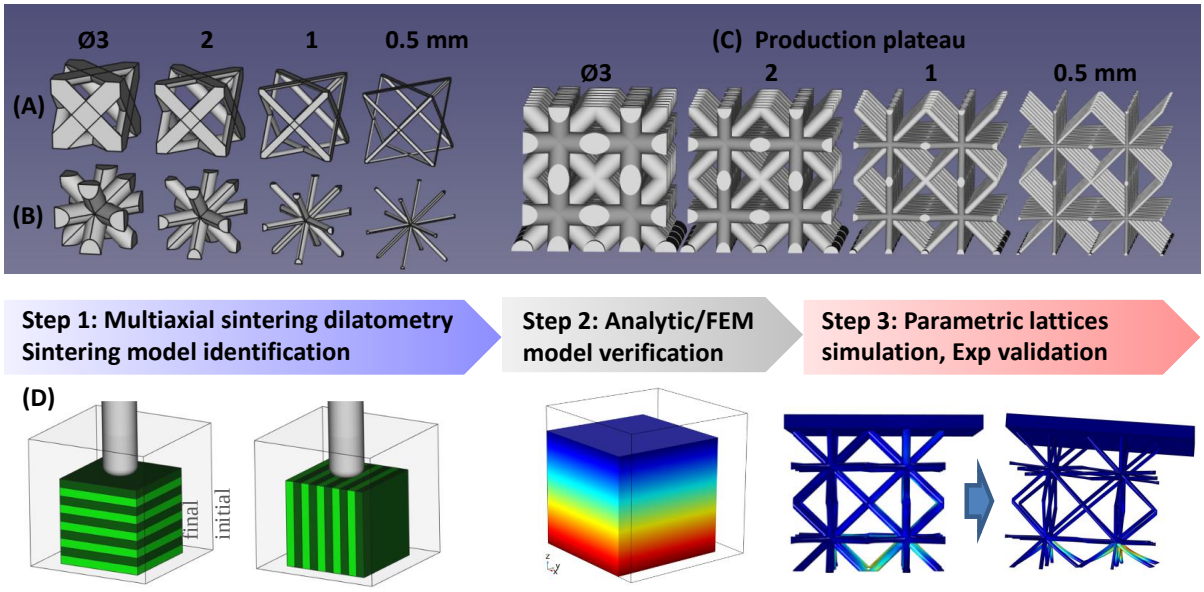

Figure 1 Design of the printed lattice structures with (A) the starting unit cells with rod diameters from 3 to 0.5mm, (B) the equivalent cells with full-rod diameter and (C) the view of the printer plateau with the replicated lattices structures; below (D) the article main steps for the model identification, validation and parametric lattice simulation is presented.

3. Theory and calculations

Simulate by FEM method the sintering of 3D printed specimens use continuum based sintering models. In this study Olevsky's model was used [27]. A realistic sintering model of green printed specimens should simulate the sintering shrinkage anisotropy. Below sections are dedicated to the sintering model description and the identification method.

3.1. Sintering equations

The sintering behavior relates the stress, strain rate tensors and the sintering stress of a compressible medium by the following general equation for pressureless sintering [27,28]:

$$\underline{\sigma} = 2\eta\left(\varphi\underline{\dot{\varepsilon}} + \left(\psi - \frac{1}{3}\varphi\right)\dot{e}\,\underline{\underline{\mathbb{1}}}\right) + P_l\,\underline{\underline{\mathbb{1}}} \qquad (1).$$

In above equation, P_l is the sintering stress that originates from the capillarity forces at the grain surface. If simple shapes are used, we have $\underline{\sigma}$=0 and P_l is the main diving force of sintering. However, in the case of thin lattices, the weight of the top plate coupled to the very thin supporting structure makes non-negligible stress ($\underline{\sigma}\neq 0$) in the thin structures which can result in distortions. The viscosity η can be defined by the general Arrhenius form [38]:

$$\eta = \eta_0 T \exp(\frac{Q}{RT}) \quad (2).$$

The shear and bulk modulus (φ and ψ) model porous skeleton behavior and are functions of the porosity. The moduli functions can be theoretically approximated by Skorohod's model [27,39]:

$$\varphi = (1-\theta)^2 \quad (3)$$

$$\psi = \frac{2}{3}\frac{(1-\theta)^3}{\theta} \quad (4).$$

A similar expression of the sintering model gathers the viscosity and the moduli defining effective shear and bulk viscosities [27,40].

$$\underline{\sigma} = \left(K\dot{e}\mathbb{i} + 2G\left(\underline{\dot{\varepsilon}} - \frac{1}{3}\dot{e}\mathbb{i}\right)\right) + P_l\mathbb{i} \quad (5)$$

In the later equation, the expression of the shear and bulk viscosities are $G = \eta\varphi$ and $K = 2\eta\psi$ respectively.

The porosity elimination rate $\dot{\theta}$ and the rate of volumetric directional changes $\dot{e}$ are related by mass conservation equation.

$$\frac{\dot{\theta}}{1-\theta} = \dot{\varepsilon}_x + \dot{\varepsilon}_y + \dot{\varepsilon}_z = \dot{e} \quad (6)$$

3.2. Anisotropic pressureless sintering model identification

3D printed specimens have more interlayer porosity resulting in more sintering shrinkage in the building direction. This anisotropy of the sintering shrinkage involves different changes in the sintering model (1). The architected porosity distribution (reported in figure 2) implies different properties in the building direction (axe Z) and in radial directions (axes R in the layer direction) and weaker shear resistance between the layers. In the sintering model (1), the shear and bulk moduli (or alternatively the effective shear and bulk viscosities) and the sintering stress should be anisotropic. However, identify separately all these parameters are very difficult as it implies different specific tests to distinguish all the anisotropic shear and bulk behaviors like sinter-forging, shear, triaxial tests, with and without loading. In the literature, this complex behavior[41] is simplified by different approaches requiring only simple dilatometry tests. In a first common approach, the anisotropic sintering stress (Pl) is

used to fit the experimental specimen dimensions[27,42,43]. In general, this approach assumes a mechanistic model with equivalent ellipsoidal porosity or grains to justify different directional driving forces[42,44]. Another approach applies the anisotropy directly at the level of the strain rate[31]. Finally, it is possible to apply the anisotropy at the level of the shear and bulk viscosities[29,32,45] which imply anisotropic porous skeleton. All previously cited approaches allow simulating the shrinkage of green printed shapes. However, the latter method is preferred because in addition to the shrinkage, it allows to better reproduce the inherent anisotropic sintering resistance to deformation (*via* the effective anisotropic shear and bulk viscosities).

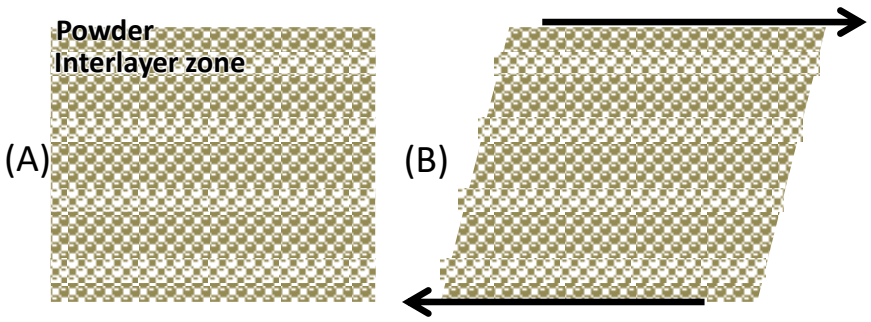

Figure 2 Scheme of the architected porosity from the 3D printing process (A), illustration of the weak deformation behavior in the case of shear solicitation parallel to the layers (B).

In a previous article[29], we developed an analytic model able to model the anisotropic sintering shrinkage of a regular shape specimen. An identification method of the effective anisotropy parameters was proposed. The first step consists of plotting the linear regression of the effective viscosity terms (Yr and Yz) in Z and R axes *vs* 1/(RT) using the following equations.

$$Yr = ln\left(\frac{-3(1-\theta)^2}{2Tr\left(\dot{\varepsilon}_r+\dot{\varepsilon}_z\frac{\left(\psi-\frac{\varphi}{3}\right)}{\left(2\psi+\frac{\varphi}{3}\right)}\right)\left(2\psi+\frac{\varphi}{3}\right)}\right) = ln\left(\frac{\eta_{0r}}{\alpha}\right)+\frac{Q}{RT} \quad (7)$$

$$Yz = ln\left(\frac{-3(1-\theta)^2}{2Tr\left(\dot{\varepsilon}_z+2\dot{\varepsilon}_r\frac{\left(\psi-\frac{\varphi}{3}\right)}{\left(\psi+\frac{2\varphi}{3}\right)}\right)\left(\psi+\frac{2\varphi}{3}\right)}\right) = ln\left(\frac{\eta_{0z}}{\alpha}\right)+\frac{Q}{RT} \quad (8)$$

The slope gives the activation energy Q that should converge to the same value. Then, the effective viscosities pre-exponent factors ($\eta_{0r}(\theta), \eta_{0z}(\theta)$) are plotted *vs* the porosity knowing the activation energy, the dilatometry experimental data ($\theta, T, \dot{\varepsilon}_r, \dot{\varepsilon}_z$) and assuming modified Skorohod's moduli expressions (φ, ψ). The following equations are used.

$$\frac{-3(1-\theta)^2}{2r\left(\dot{\varepsilon}_r+\dot{\varepsilon}_z\frac{\left(\psi-\frac{\varphi}{3}\right)}{\left(2\psi+\frac{\varphi}{3}\right)}\right)\left(2\psi+\frac{\varphi}{3}\right)\mathrm{Texp}\left(\frac{Q}{RT}\right)}=\frac{\eta_{0r}(\theta)}{\alpha} \quad (9)$$

$$\frac{-3(1-\theta)^2}{2r\left(\dot{\varepsilon}_z+2\dot{\varepsilon}_r\frac{\left(\psi-\frac{\varphi}{3}\right)}{\left(\psi+\frac{2\varphi}{3}\right)}\right)\left(\psi+\frac{2\varphi}{3}\right)\mathrm{Texp}\left(\frac{Q}{RT}\right)}=\frac{\eta_{0z}(\theta)}{\alpha} \quad (10)$$

Generally, the expression of $\eta_{0r}(\theta)$ and $\eta_{0z}(\theta)$ evolves with the porosity from a significant anisotropy at high porosity to an isotropic shrinkage rate when approaching the full elimination of the porosity. The anisotropy is introduced at the level of the term $\eta_{0r}(\theta)$ where an additional function "*f*" is added. A vanishing anisotropy behavior ($f(\theta)\rightarrow 0$ for $\theta\rightarrow 0$) is expected as the origin of the anisotropy is an architected porosity which is eliminated during the sintering.

4. Results and discussions

In this section, the powder, sintered microstructures and dilatometry tests are first analyzed. Then, the identification of the anisotropic sintering behavior is investigated and the resulting parameters are verified by analytical modeling and FEM simulations. Finally, the FEM simulation of the lattices loaded by the plate is conducted and compared to the experiment.

4.1. Starting powder analysis

In order to characterize the starting alumina powder, the ceramic resin has been debinded at 600°C in air to remove the organic without sintering of the powder. The SEM image of the powder is reported in figure 3 with the particle size distribution. The powder is highly bimodal with a main part of the grains between 100-600 nm and bigger grains ranging between 1-2.5 µm. This bimodal distribution is often used in ceramic stereolithography to

increase the green density of the printed parts[8]. The initial average particle size is 0.367 µm. This value has been taken as an initial average particle diameter in the following sintering model calculations.

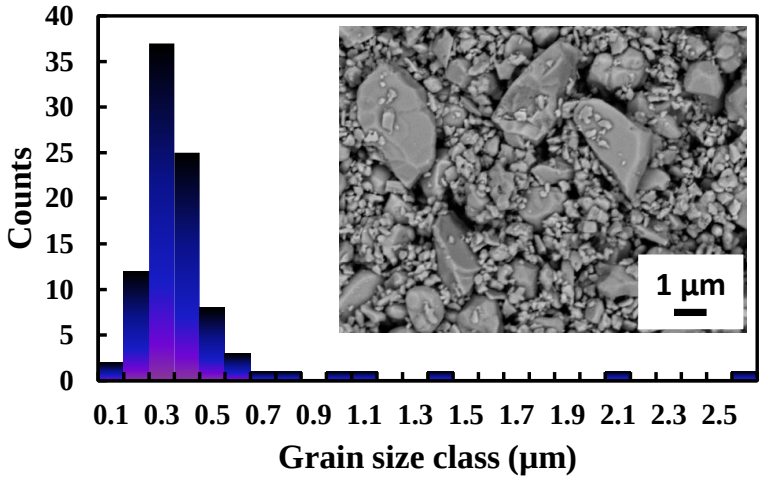

Figure 3 SEM image of the debinded ceramic cream at 600°C in air and histogram of the particle diameter distribution.

4.2. Sintering dilatometry and microstructure

The scheme of the dilatometry experiments in the building direction "Z" and in the other radial directions "R" configurations are reported in figure 4a. The SEM image of the printed surface showing the 50 µm layer architecture is reported in figure 4b. The debinding/pre-consolidation cycle implies 18.3% loss of the initial mass and respectively 0.7 and 2.1% of shrinkage in the layers thickness (Z axis) and layer plane (R axis). Finally, the sintering shrinkage curves of the 5 mm cube are presented in figure 4c. The latter shows the sintering shrinkage is 3 % higher in the building direction and the sintering anisotropy starts near 1300°C. The shrinkage curves indicate that the densification is stopped at the very end of the 3 h dwell at 1600°C. This points out that the sintering cycle is well optimized. These data will be used for the identification of the sintering model. The initial relative density is 59%. This high value is due to the powder mix with large grains (figure 3) that improve the initial powder tap density.

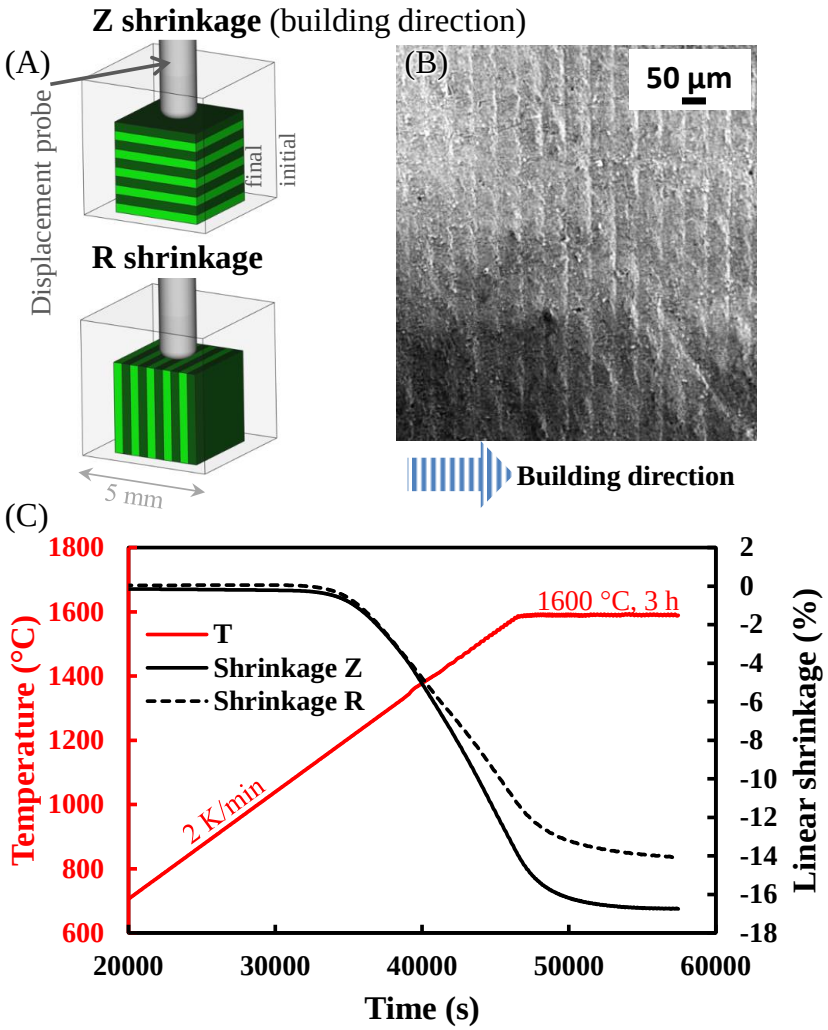

Figure 4 dilatometry configuration (A), SEM of the printed specimen surface (B), sintering dilatometry of the curves (C).

The SEM image of the sintered alumina ceramic is reported in figure 5. The image at 50× of magnification shows the overall densification with the presence of a few porosity resulting from bubbles at the scraping process and small porosity at the interlayer zone. The latter image also shows the layered surface aspect of the printed and sintered specimen. The image at 1500× of magnification shows the microstructure with grains slightly elongated in the layer direction. This is probably due to a preferential orientation of the bigger grains (figure 3) during the scraping. The average grain size is 3.22 µm and the image shows the residual porosity estimated to 3.90% from Archimedes's density measurement.

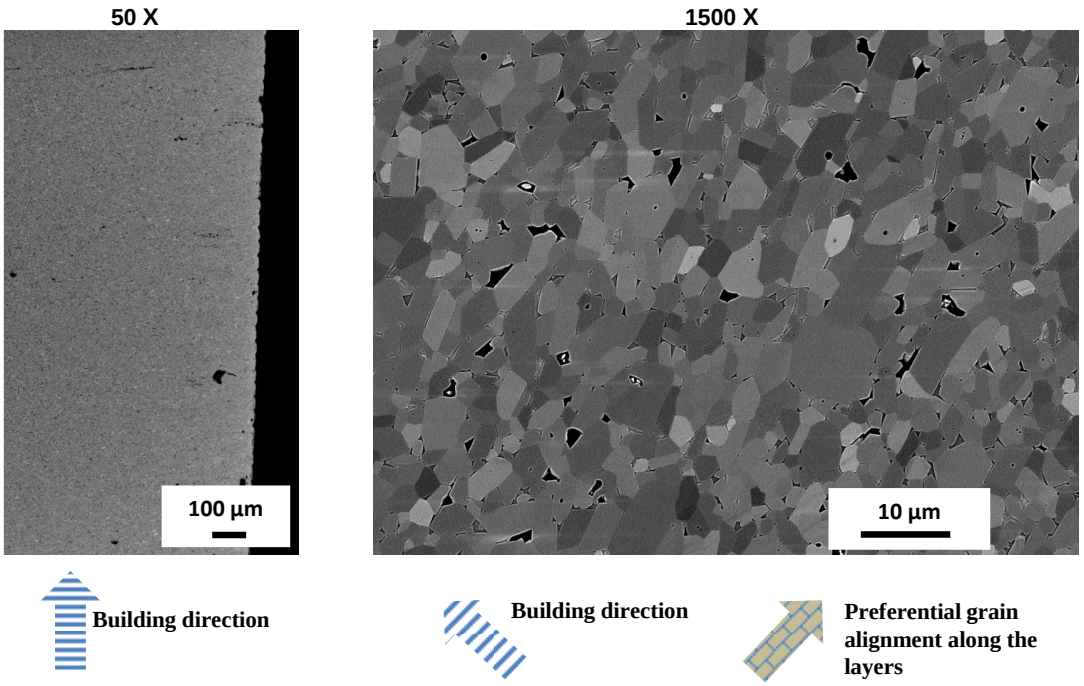

Figure 5 Sintered microstructure of 3D printed alumina specimens.

4.3. Identification of the anisotropic sintering modeling parameters

Based on the dilatometry data in the R and Z configurations (figure 4) the specimen height evolutions $h_Z(t)$ and $h_R(t)$ were determined and the sintering strain rates in both directions have been extracted with the expressions $\dot{\varepsilon}_z = \dot{h}_z/h_z$, $\dot{\varepsilon}_R = \dot{h}_R/h_R$. The obtained strain rates are reported in Figure 6a. This shows that below 1300°C, the densification is nearly isotropic in shrinkage rate, between 1300°C and 1h of holding at 1600°C, the anisotropy is strong and it becomes again isotropic in the middle of the holding. With the experimental data $(\theta, T, \dot{\varepsilon}_r, \dot{\varepsilon}_z)$ the regression equations (7) and (8) have been plotted in figure 6b. The shear and bulk moduli used in these calculations are the Skorohod theoretical moduli with a correction of the initial and final critical porosity[46,47]. The used expressions are detailed below.

$$\psi = \left(\frac{2}{3}\right)\frac{(0.5-\theta)^3}{(\theta-0.02)} \qquad (11)$$

$$\varphi = \left(1-\frac{\theta}{0.5}\right)^2 \qquad (12)$$

As expected, the temperature behavior is unique and the two curves converge to the same activation energy of 360 kJ/mol. From the activation energies provided in the deformation mechanisms map of alumina[48], this activation energy suggests a grain boundary diffusion

mechanism as it is close to the value of 380 kJ/mol for grain boundary diffusion of oxygen and far from the value of 636 kJ/mol for lattice diffusion.

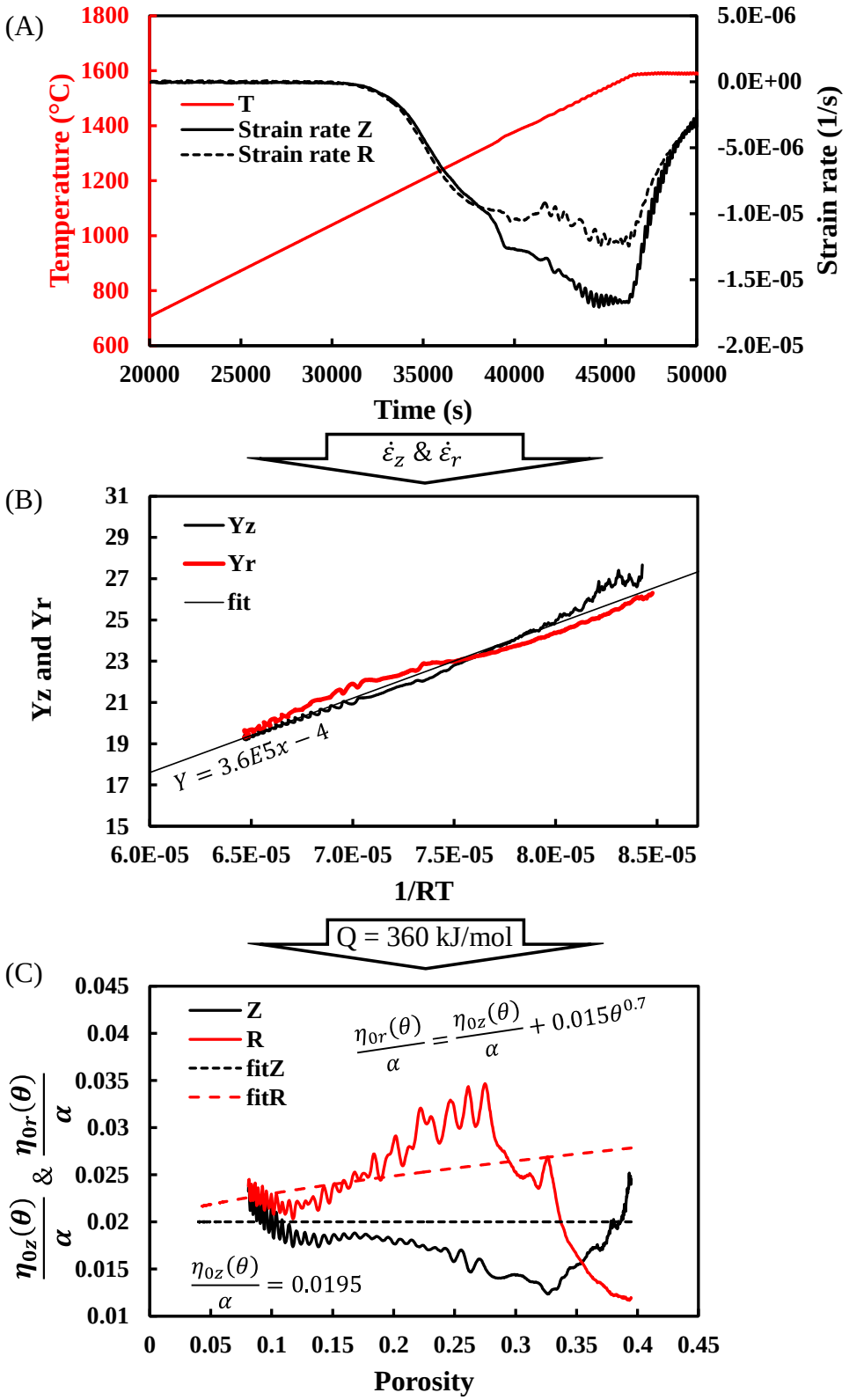

Figure 6 Experimental strain rate in Z and R directions (A), linear regression of Yz and Yr, for extraction of the sintering activation energy (B), identification of the viscosity pre-exponential parameters vs porosity (C).

The experimental evolution of the pre-exponential factors is reported in figure 6c *vs* porosity. The curves oscillations are due to a few degree temperature oscillations in the PID regulation (see figure 6a). The functions of $\eta_{0r}(\theta)$ and $\eta_{0z}(\theta)$ divided by α (1.12 J/m^2 for alumina[38]) reflects the anisotropy of the shear and bulk moduli by their difference in Z and R directions. As expected by the dilatometry curves, the shrinkage rate is significantly anisotropic in intermediate stage sintering and slowly becomes isotropic at the very end of sintering. These curves can be implemented directly in the FEM model. However, the high noise of these curves will imply calculation instabilities requiring to model these curves by the anisotropy function "f" previously cited. The latter is added to the radial fitted term η_{0r} that has the form $\eta_{0r} = \eta_{0Z} + f$; this decreases the shrinkage in the radial direction. We use this approach in a previous study on the sintering anisotropy of robocasting printed specimens[32]. Here the value of η_{0Z} is nearly constant and the function $f = 0.015\theta^{0.7}$ was used. For simplicity, the fitting functions do not match the pre-exponent values in the high porosity zone because at initial stage sintering, the sintering is slow and the errors on the modeled curves are negligible. The fitting curves in figure 6c have been adjusted to have a good prediction of the experimental dilatometric data. An analytic sintering model with calculation time as short as 20s has been developed previously [29] to conduct such fine adjustments. In the present case, the fitting parameters have been slowly adjusted to explain the experimental pre-exponents (in figures 6c) and to have a good prediction of the sintering data reported in figure 7.

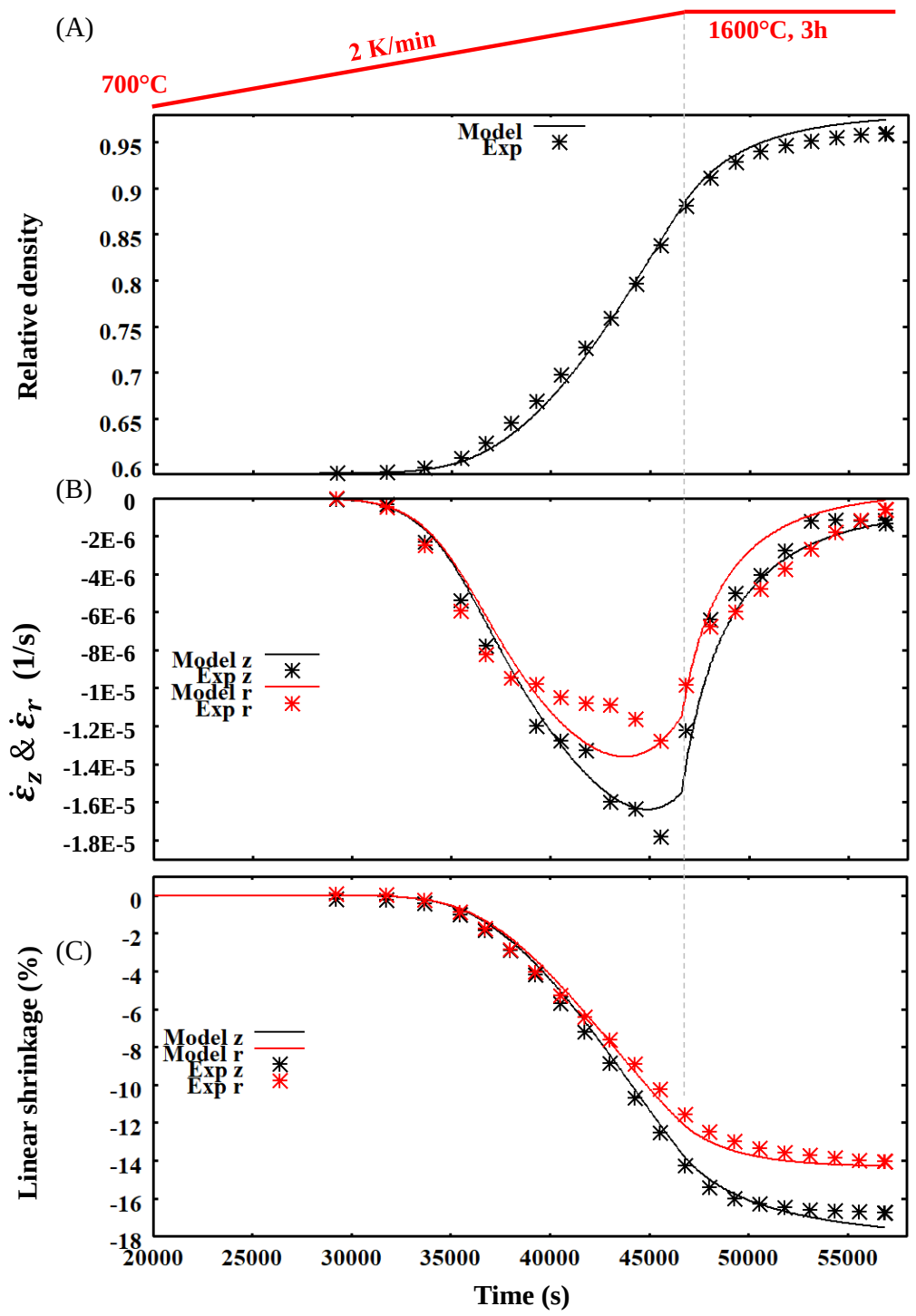

Figure 7 Analytic sintering modeling of the experimental dilatometric data.

4.4. Verification of FEM sintering model using the identified parameters

At this stage, the sintering model is fully identified. The identified sintering parameters (Q, η_{0r},η_{0z}, φ and ψ) can be implemented in the FEM model. Before starting to simulate the lattice sintering, the 5 mm cube sintering was tested to verify if the FEM model gives coherent results compared to the analytic sintering model and the experimental data. The

simulated 5 mm cube and relative density curves are reported in figure 8a. Similarly, the simulated linear shrinkage is reported in figure 8b. The FEM simulation reproduces well experimental and analytical solutions. The error in sintering and dimensional results is less than 1% compared to the analytical case and 4% for the final "Z" shrinkage compared to experiment.

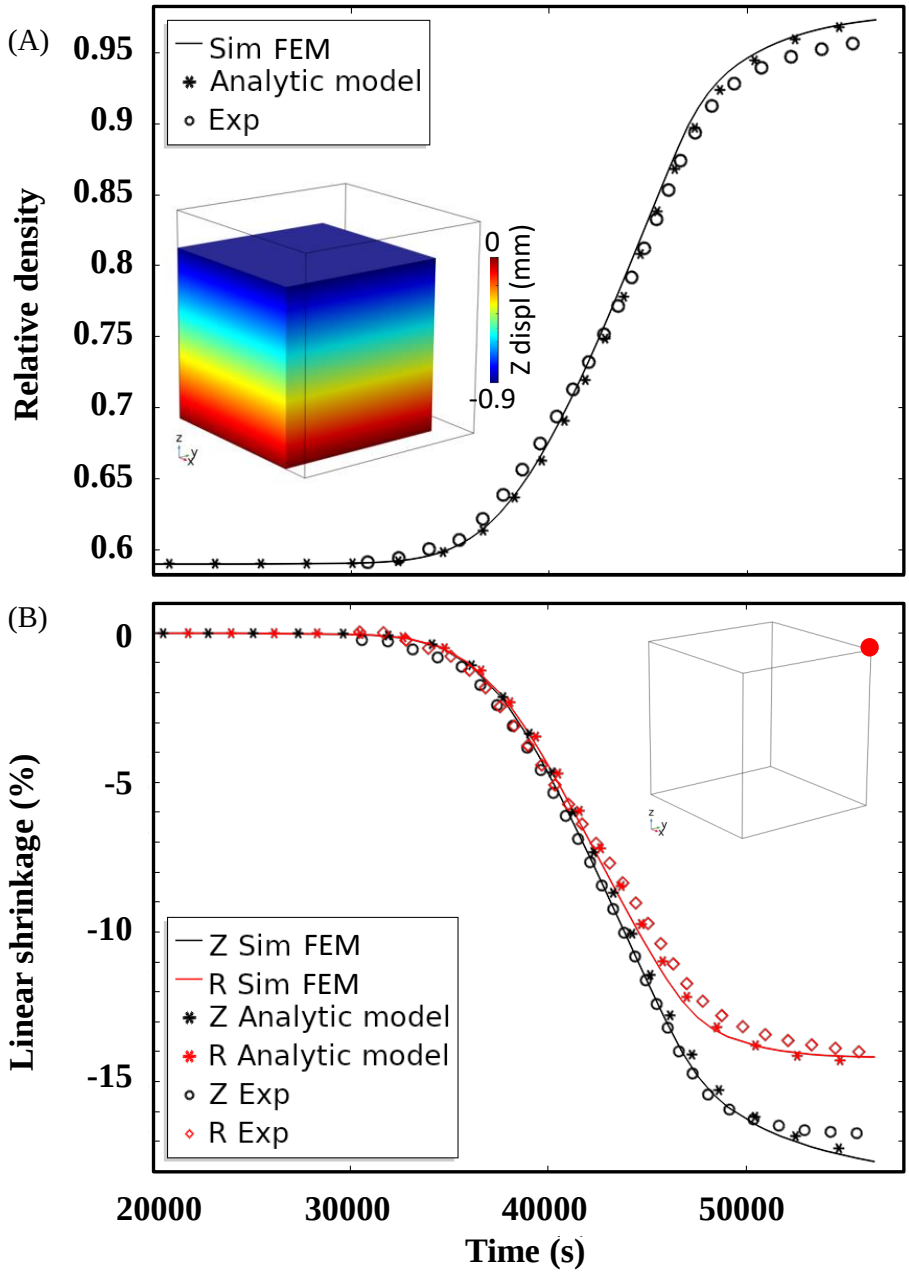

Figure 8 FEM simulation of the dilatometric experiment and comparison of the analytic, FEM and experimental data with: (A) the relative density, the 3D view of Z displacement is reported in insert , (B) the sintering shrinkage, the location of the virtual measurement probe is reported in insert.

4.5. Initial description of the lattices sintering FEM simulation

The aim of this study is to detect the critical rod diameter where severe distortions appear. Consequently, the loaded printed lattices (represented in figure 1c) with rod diameters from 3 to 0.5 mm are simulated using the same dilatometry cycle and used the initial CAD shapes. The few % of pre-consolidation shrinkage are neglected. In a first time, the two extreme lattices cases are discussed to detect the main interesting comparison characteristics, then, the parametric lattice analysis (with different rod diameters) is described after.

In figure 9, the two extreme lattices with rod diameters of 3 and 0.5 mm are presented. The experimental relative shrinkage of the cube is presented as a reference. If unwanted macroscopic distortions result the lattice fragile structure, the simulated shrinkage will be far from the cube shrinkage. This shows that the lattice having a strong structure with 3 mm thick rod has a very predictable sintering with a shrinkage percent that corresponds to the 5 mm cube case, no undesired deformations and developed von Mises stress as low as 4E-3 MPa. On the contrary, the thin lattice structure with 0.5 mm rod diameter undergoes severe distortions with 12% additional Z axis shrinkage compared to the small cube case and a developed von Mises stress as high as 2 MPa.

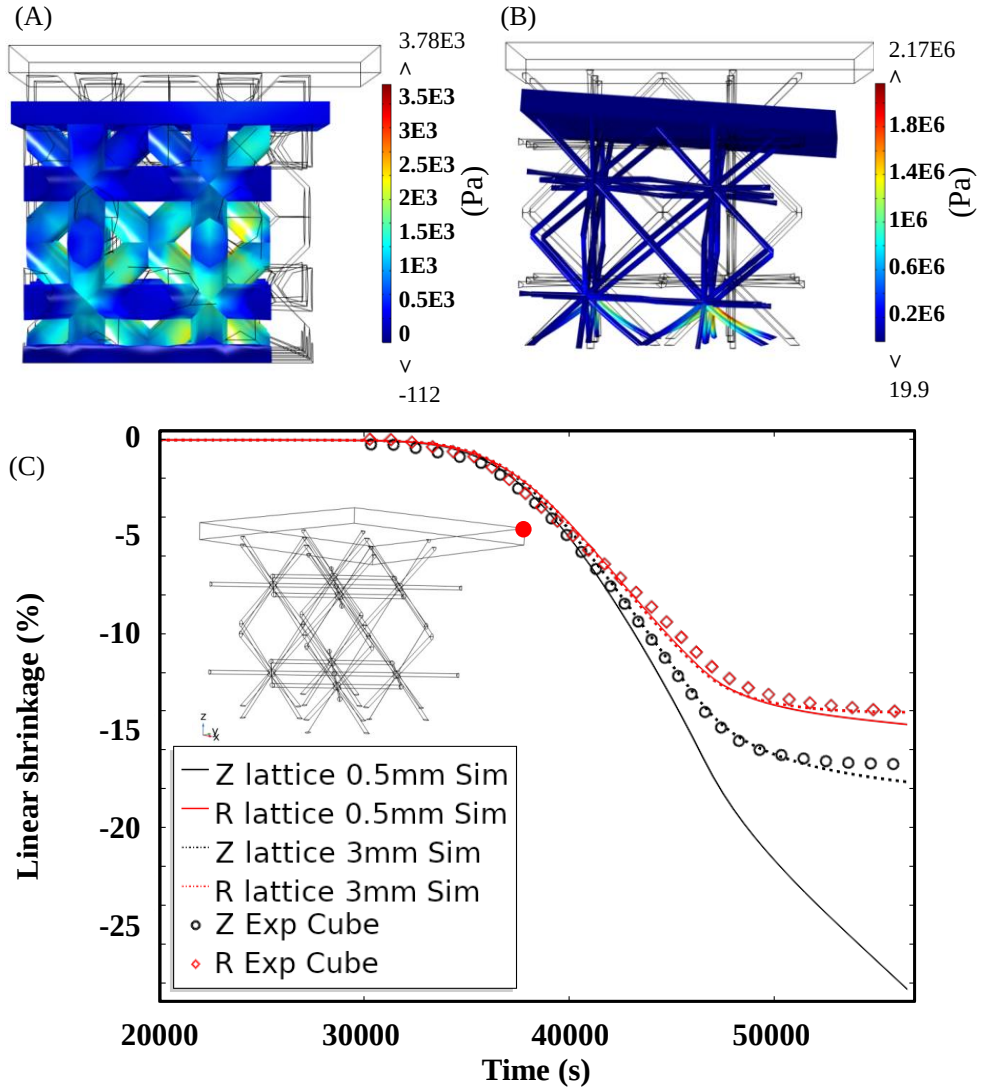

Figure 9 FEM simulation of the lattices structure with a rod diameter of 3 mm (A) and 0.5 mm (B), for the two simulations, a virtual displacement probe is placed (red point) to record the Z and R linear shrinkages (C), the experimental value of the 5 mm cube dilatometry shrinkage is also plotted to estimate the level of undesired sintering distortion.

4.6. Parametric simulation of the lattices rod thickness and experimental comparison

The main objective of this study is to detect the critical lattice rod diameter at which the lattice undergoes severe distortions and to verify the capacity of the FEM model to predict this lattice resistance threshold. All the tested lattices and corresponding FEM simulations are reported in figure 10. The photo of the debinded lattices (figure 10a) shows the quality of the printing able to produce strong structures as well as very fragile lattices containing weak supported zones. The main printing defects are at the level of the supports where the shape ejection implies some defects; small delaminations are present in some rod junctions and at

the level of the horizontal unsupported zones. The latter zones make some distortions after debinding for the 0.5 mm case. After sintering (figure 10b), the delaminations in the unsupported zone are slightly increased. Experimentally, the severe distortion appears only in the 0.5 mm lattice. The FEM simulation at the end of the sintering (figure 10c) confirms the appearance of severe lattice distortions only for the 0.5 mm lattice. The simulation allows plotting the maximum lattices developed von Mises stresses and the distortions (see figure 10d). This shows the deformation zone is present above the 0.1 MPa of developed stress in the structure. The FEM model succeeds in predicting the severe distortion zone observed experimentally. For the 0.5 mm lattice, the predicted distortion is less important than the experimental case. This is explained by the printing defects like the delamination that decrease the shape resistance to distortions. Moreover, the model do not simulate the stage of cracks formation, it is used to model the sintering distortions and detect the onset of severe distortions. This points out the necessity to take a margin in the predicted lattice resistance obtained by FEM simulations that assumes no defects from the printing process.

Nevertheless, the predictability of the FEM model is very satisfactory to detect the lattice resistance threshold for topology optimization tool[16,49]. A prospect for latter application can be to use the FEM model to identify effective continuum materials that mimic the weaker high temperature behavior of lattices. Such materials will significantly reduce the calculation time compared to the case where the lattice themselves are simulated. A similar approach is used to study the multiscale porosity behavior of some ceramics[50].

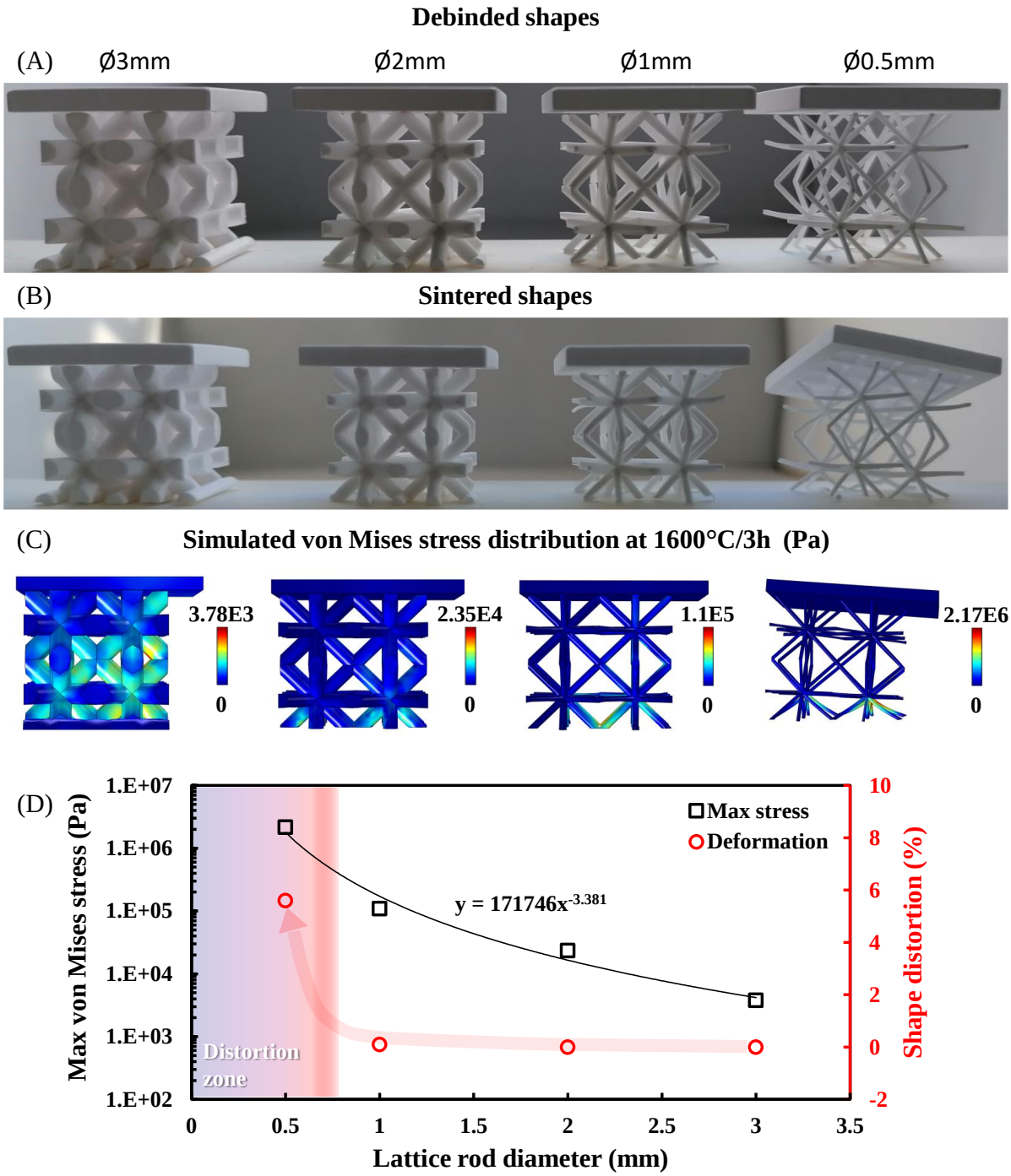

Figure 10 Photo of the debinded lattices structures (A), photo after sintering at 1600°C, 3 h (B), FEM simulated corresponding lattices at the end of sintering (C), plotted maximum shape deformation and von Mises stress developed (D).

5. Conclusion and prospects

Thin lattice structures are used as support materials or filling materials in bioinspired lightweight parts having high mechanical/functional performances and multiscale structures. These structures are developed with 3D printer slicer software and with advance topological optimization tools that improve the design of thick parts. However, these numerical tools do not include the high temperature weaker resistance of lattices during the sintering. In this work, a first step is made to predict by FEM simulations the printed thin structure resistance to sintering distortions. An experimental protocol is proposed to extract the high temperature sintering behavior of the stereolithography printed specimens and to implement these data in a fast computation analytic model and then in a FEM simulation tool to predict the lattice sintering behavior. In particular, the sintering behavior has to include the sintering anisotropy of printed ceramics where higher shrinkage is observed in the building direction.

This study shows that very thin, low density and complex alumina lattices can be produced by ceramic stereolithography. The investigated lattices contain weakly supported structures and rod diameter structures down to 0.5 mm for filling density as low as 1.6 vol%. These very challenging lattices structures explore both the 3D printer and the sintering resistance tests to their limit. All the lattice structures were successfully printed and only a few delamination was observed in the horizontal cantilever zones. The experimental lattice sintering tests show the distortion resistance threshold immediately before the weakest lattice (1.6vol%) that undergoes severe sintering distortions. The FEM simulation succeeds in predicting the severe deformation zones observed experimentally.

This work offers many positive prospects.

(i) The immediate prospect is the possibility to use the FEM tool to predict lattice high temperature stress resistance threshold in replacement from the room temperature properties used in topological optimization approaches.

(ii) Still in topology optimization, the FEM model can be used to identify equivalent continuum material properties that behave like the lattices but with a significant reduction of the calculation cost.

(iii) This article modeling approach can be used to simulate the sintering behavior of bioinspired 3D printed objects with internal or external lattices structures.

Acknowledgements

The help and support of Christophe Couder, Christelle Bilot and Jérôme Lecourt is gratefully acknowledged. This work was supported by: the French National Research Agency (ANR), project ULTRARAPIDE N°ANR-19-CE08-0033-01 and the project "région normadie" - 00016601-20E02057_RIN RECHERCHE 2020 - Emergent – ULTIMODULUS.

References

[1] R.L. Truby, J.A. Lewis, Printing soft matter in three dimensions, Nature. 540 (2016) 371–378. doi:10.1038/nature21003.

[2] T. Chartier, A. Badev, Rapid Prototyping of Ceramics, in: Handb. Adv. Ceram., Elsevier, 2013: pp. 489–524. doi:10.1016/B978-0-12-385469-8.00028-9.

[3] Y. Lakhdar, C. Tuck, J. Binner, A. Terry, R. Goodridge, Additive manufacturing of advanced ceramic materials, Prog. Mater. Sci. 116 (2021) 100736. doi:10.1016/j.pmatsci.2020.100736.

[4] J. Deckers, J. Vleugels, J.P. Kruth, Additive Manufacturing of Ceramics: A Review, J. Ceram. Sci. Technol. 5 (2014) 245–260. doi:10.4416/JCST2014-00032.

[5] Z. Chen, Z. Li, J. Li, C. Liu, C. Lao, Y. Fu, C. Liu, Y. Li, P. Wang, Y. He, 3D printing of ceramics: A review, J. Eur. Ceram. Soc. 39 (2019) 661–687. doi:10.1016/j.jeurceramsoc.2018.11.013.

[6] P.J. Bártolo, Stereolithography, Springer US, Boston, MA, 2011. doi:10.1007/978-0-387-92904-0.

[7] F. Kotz, K. Arnold, W. Bauer, D. Schild, N. Keller, K. Sachsenheimer, T.M. Nargang, C. Richter, D. Helmer, B.E. Rapp, Three-dimensional printing of transparent fused silica glass, Nature. 544 (2017) 337–339. doi:10.1038/nature22061.

[8] I.L. de Camargo, M.M. Morais, C.A. Fortulan, M.C. Branciforti, A review on the rheological behavior and formulations of ceramic suspensions for vat photopolymerization, Ceram. Int. 47 (2021) 11906–11921. doi:10.1016/j.ceramint.2021.01.031.

[9] H. Wu, Y. Cheng, W. Liu, R. He, M. Zhou, S. Wu, X. Song, Y. Chen, Effect of the particle size and the debinding process on the density of alumina ceramics fabricated by 3D printing based on stereolithography, Ceram. Int. 42 (2016) 17290–17294.

doi:10.1016/j.ceramint.2016.08.024.

[10] H. Li, L. Song, J. Sun, J. Ma, Z. Shen, Dental ceramic prostheses by stereolithography-based additive manufacturing: potentials and challenges, Adv. Appl. Ceram. 118 (2019) 30–36. doi:10.1080/17436753.2018.1447834.

[11] C.-J. Bae, J.W. Halloran, Influence of Residual Monomer on Cracking in Ceramics Fabricated by Stereolithography, Int. J. Appl. Ceram. Technol. 8 (2011) 1289–1295. doi:10.1111/j.1744-7402.2010.02578.x.

[12] Y. Liu, L. Zhan, Y. He, J. Zhang, J. Hu, L. Cheng, Q. Wu, S. Liu, Stereolithographical fabrication of dense Si3N4 ceramics by slurry optimization and pressure sintering, Ceram. Int. 46 (2020) 2063–2071. doi:10.1016/j.ceramint.2019.09.186.

[13] C.W. Hull, Method for production of three-dimensional objects by stereolithography, US5762856A, 1998. www.google.com/patents/US4929402.

[14] T. Chartier, C. Duterte, N. Delhote, D. Baillargeat, S. Verdeyme, C. Delage, C. Chaput, Fabrication of Millimeter Wave Components Via Ceramic Stereo- and Microstereolithography Processes, J. Am. Ceram. Soc. 91 (2008) 2469–2474. doi:10.1111/j.1551-2916.2008.02482.x.

[15] M. Orme, I. Madera, M. Gschweitl, M. Ferrari, Topology Optimization for Additive Manufacturing as an Enabler for Light Weight Flight Hardware, Designs. 2 (2018) 51. doi:10.3390/designs2040051.

[16] J. Zhu, H. Zhou, C. Wang, L. Zhou, S. Yuan, W. Zhang, A review of topology optimization for additive manufacturing: Status and challenges, Chinese J. Aeronaut. 34 (2021) 91–110. doi:10.1016/j.cja.2020.09.020.

[17] A. du Plessis, C. Broeckhoven, I. Yadroitsava, I. Yadroitsev, C.H. Hands, R. Kunju, D. Bhate, Beautiful and Functional: A Review of Biomimetic Design in Additive Manufacturing, Addit. Manuf. 27 (2019) 408–427. doi:10.1016/j.addma.2019.03.033.

[18] J.A. Hawreliak, J. Lind, B. Maddox, M. Barham, M. Messner, N. Barton, B.J. Jensen, M. Kumar, Dynamic Behavior of Engineered Lattice Materials, Sci. Rep. 6 (2016) 28094. doi:10.1038/srep28094.

[19] A. Velasco-Hogan, J. Xu, M.A. Meyers, Additive Manufacturing as a Method to Design and Optimize Bioinspired Structures, Adv. Mater. 30 (2018) 1800940. doi:10.1002/adma.201800940.

[20] Y. Yang, X. Song, X. Li, Z. Chen, C. Zhou, Q. Zhou, Y. Chen, Recent Progress in Biomimetic Additive Manufacturing Technology: From Materials to Functional Structures, Adv. Mater. 30 (2018) 1706539. doi:10.1002/adma.201706539.

[21] Q. Zhang, X. Yang, P. Li, G. Huang, S. Feng, C. Shen, B. Han, X. Zhang, F. Jin, F. Xu, T.J. Lu, Bioinspired engineering of honeycomb structure – Using nature to inspire human innovation, Prog. Mater. Sci. 74 (2015) 332–400. doi:10.1016/j.pmatsci.2015.05.001.

[22] Y. Zhang, F. Zhang, Z. Yan, Q. Ma, X. Li, Y. Huang, J.A. Rogers, Printing, folding and assembly methods for forming 3D mesostructures in advanced materials, Nat. Rev. Mater. 2 (2017) 17019. doi:10.1038/natrevmats.2017.19.

[23] X. Xia, C.M. Spadaccini, J.R. Greer, Responsive materials architected in space and time, Nat. Rev. Mater. 7 (2022) 683–701. doi:10.1038/s41578-022-00450-z.

[24] J. Jiang, X. Xu, J. Stringer, Support Structures for Additive Manufacturing: A Review, J. Manuf. Mater. Process. 2 (2018) 64. doi:10.3390/jmmp2040064.

[25] T. Schlordt, F. Keppner, N. Travitzky, P. Greil, Robocasting of Alumina Lattice Truss Structures, J. Ceram. Sci. Technol. 03 (2012) 81–88. doi:10.4416/JCST2012-00003.

[26] S. Sadeghi Borujeni, A. Shad, K. Abburi Venkata, N. Günther, V. Ploshikhin, Numerical simulation of shrinkage and deformation during sintering in metal binder jetting with experimental validation, Mater. Des. 216 (2022) 110490. doi:10.1016/j.matdes.2022.110490.

[27] E.A. Olevsky, Theory of sintering: from discrete to continuum, Mater. Sci. Eng. R Reports. 23 (1998) 41–100. doi:10.1016/S0927-796X(98)00009-6.

[28] R.K. Bordia, S.-J.L. Kang, E.A. Olevsky, Current understanding and future research directions at the onset of the next century of sintering science and technology, J. Am. Ceram. Soc. 100 (2017) 2314–2352. doi:10.1111/jace.14919.

[29] C. Manière, G. Kerbart, C. Harnois, S. Marinel, Modeling sintering anisotropy in ceramic stereolithography of silica, Acta Mater. 182 (2020) 163–171. doi:10.1016/j.actamat.2019.10.032.

[30] Q. Li, W. Hou, J. Liang, C. Zhang, J. Li, Y. Zhou, X. Sun, Controlling the anisotropy behaviour of 3D printed ceramic cores: From intralayer particle distribution to interlayer pore evolution, Addit. Manuf. 58 (2022) 103055. doi:10.1016/j.addma.2022.103055.

[31] P. Kakanuru, K. Pochiraju, Simulation of shrinkage during sintering of additively manufactured silica green bodies, Addit. Manuf. 56 (2022) 102908. doi:10.1016/j.addma.2022.102908.

[32] C. Manière, C. Harnois, S. Marinel, 3D printing of porcelain: finite element simulation of anisotropic sintering, Int. J. Adv. Manuf. Technol. 116 (2021) 3263–3275. doi:10.1007/s00170-021-07304-y.

[33] L.-J. Wen, X.-G. Hu, Z. Li, Zhan-Hua Wang, J.-K. Wu, Q. Zhu, Anisotropy in tensile properties and fracture behaviour of 316L stainless steel parts manufactured by fused deposition modelling and sintering, Adv. Manuf. 10 (2022) 345–355. doi:10.1007/s40436-022-00402-4.

[34] M.A. Wagner, A. Hadian, T. Sebastian, F. Clemens, T. Schweizer, M. Rodriguez-Arbaizar, E. Carreño-Morelli, R. Spolenak, Fused filament fabrication of stainless steel structures - from binder development to sintered properties, Addit. Manuf. 49 (2022) 102472. doi:10.1016/j.addma.2021.102472.

[35] A. Cabo Rios, E. Hryha, E. Olevsky, P. Harlin, Sintering anisotropy of binder jetted 316L stainless steel: part I – sintering anisotropy, Powder Metall. 65 (2022) 273–282. doi:10.1080/00325899.2021.2020485.

[36] M. Zago, N.F.M. Lecis, M. Vedani, I. Cristofolini, Dimensional and geometrical precision of parts produced by binder jetting process as affected by the anisotropic shrinkage on sintering, Addit. Manuf. 43 (2021) 102007. doi:10.1016/j.addma.2021.102007.

[37] V. Pateloup, P. Michaud, T. Chartier, Optimization of part orientation and adapted supports for manufacturing of ceramic parts by stereolithography using finite element simulations, Open Ceram. 6 (2021) 100132. doi:10.1016/j.oceram.2021.100132.

[38] R.M. German, Sintering Theory and Practice, Wiley, Wiley, 1996. http://www.wiley.com/WileyCDA/WileyTitle/productCd-047105786X.html.

[39] V.V. Skorohod, Rheological basis of the theory of sintering, Nauk. Dumka, Kiev. (1972).

[40] H. Riedel, H. Zipse, J. Svoboda, Equilibrium pore surfaces, sintering stresses and constitutive equations for the intermediate and late stages of sintering—II. Diffusional densification and creep, Acta Metall. Mater. 42 (1994) 445–452. doi:10.1016/0956-7151(94)90499-5.

[41] R. Bordia, R. Zuo, O. Guillon, S. Salamone, J. Rodel, Anisotropic constitutive laws for sintering bodies, Acta Mater. 54 (2006) 111–118. doi:10.1016/j.actamat.2005.08.025.

[42] E. Olevsky, V. Skorohod, Deformation aspects of anisotropic-porous bodies sintering, Le J. Phys. IV. 03 (1993) C7-739-C7-742. doi:10.1051/jp4:19937117.

[43] B. Sarbandi, J. Besson, M. Boussuge, D. Ryckelynck, F. Barlat, Y.H. Moon, M.G. Lee, Anisotropic constitutive model and FE simulation of the sintering process of slip cast traditional porcelain, in: AIP Conf. Proc., 2010: pp. 689–696. doi:10.1063/1.3457622.

[44] A. Zavaliangos, J.M. Missiaen, D. Bouvard, Anisotropy in shrinkage during sintering, Sci. Sinter. 38 (2006) 13–25. doi:10.2298/SOS0601013Z.

[45] D. Jiang, F. Ning, Anisotropic deformation of 316L stainless steel overhang structures built by material extrusion based additive manufacturing, Addit. Manuf. 50 (2022) 102545. doi:10.1016/j.addma.2021.102545.

[46] C. Manière, T. Grippi, S. Marinel, Estimate microstructure development fromsintering shrinkage: a kinetic field approach, Mater. Today Commun. (2022).

[47] C. Manière, C. Harnois, S. Marinel, Porous stage assessment of pressure assisted sintering modeling parameters: a ceramic identification method insensitive to final stage grain growth disturbance, Acta Mater. 211 (2021) 116899. doi:10.1016/j.actamat.2021.116899.

[48] H.J. Frost, M.F. Ashby, Deformation-Mechanism Maps, The Plasticity and Creep of Metals and Ceramics, Pergamon P, Oxford, 1982. http://engineering.dartmouth.edu/defmech/.

[49] J. Wu, O. Sigmund, J.P. Groen, Topology optimization of multi-scale structures: a review, Struct. Multidiscip. Optim. 63 (2021) 1455–1480. doi:10.1007/s00158-021-02881-8.

[50] E.A. Olevsky, V. Tikare, T. Garino, Multi-Scale Study of Sintering: A Review, J. Am. Ceram. Soc. 89 (2006) 1914–1922. doi:10.1111/j.1551-2916.2006.01054.x.